Preprint of paper published by Icarus. https://doi.org/10.1016/j.icarus.2026.117298

Morphometric and Compositional Analysis of High-Slope Features in Paracelsus C, Lunar Far Side

Mark Carlotto
General Dynamics Information Systems, 553 South Street, Quincy, MA 02169

Abstract

Paracelsus C is a pre-Nectarian highland crater located within the South Pole–Aitken ejecta field. Apollo 15 panoramic photography revealed two unusual high-contrast features on the crater floor that were later resolved in Lunar Reconnaissance Orbiter Camera (LROC) imagery as two elongated high-relief structures together with a smaller nearby feature. Morphometric analyses using co-registered LROC images, QuickMap terrain products, and Lunar Orbiter Laser Altimeter (LOLA) data indicate that the two largest features are approximately 61 × 20.5 × 10.4 m and 44 × 22 × 10.2 m in size and exhibit peak slopes of 42–52°, exceeding typical slopes observed in degraded lunar highland terrains. Synthetic terrain visualizations derived from shape-from-shading reconstruction reveal textural and geometric characteristics consistent with several possible origins, including ejecta blocks, bedrock exposures, or impact-melt remnants. Regional compositional products derived from Kaguya data indicate relatively elevated olivine abundance in the vicinity of one feature, although the available datasets do not spatially resolve the individual structures. Meter-scale morphologic features are preserved in terrain exhibiting relatively low OMAT values consistent with mature surface materials. Topographic diffusion modeling suggests characteristic smoothing timescales of order 10–20 My for reconstructed meter-scale relief under published lunar diffusivities. The combined observations indicate unusually well-preserved topography whose origin remains uncertain and warrant further investigation using higher-resolution topographic, compositional, and imaging data.

Keywords: Moon; Lunar highlands; South Pole–Aitken (SP–A) basin; Geomorphology; Topographic diffusion;

Introduction

Paracelsus C is a highland crater located within the South Pole–Aitken (SP–A) ejecta field. Apollo 15 panoramic photography (Figure 1) revealed two high-contrast features on its floor that were later re-imaged by the Lunar Reconnaissance Orbiter Camera (LROC). Typically, features that appear unusual in older, lower resolution photographs turn out to be unremarkable in higher resolution digital images. This turned out not to be the case as LROC revealed two well-resolved high-relief features plus a third smaller feature (Figure 2) not evident in the Apollo photography (Carlotto et al. 2016). Independent unsupervised image surveys found the appearance of these features to be different from the background statistics of the surrounding terrain (Carlotto 2026) and from other lunar surface features (Kelahan et al. 2025).

The present-day morphology of the lunar surface is the cumulative result of impact processes and early volcanism modified over time by gravity-driven and space-weathering mechanisms that gradually degrade topography. Mass wasting is responsible for a variety of surface features (Xiao et al 2013) such as rockfalls where individual boulders break free from steep topographic features such as crater central peaks and rims and tumble downslope, debris flows of fine-grained granular material and rock fragments, slumps and slides where bedrock and regolith slide downward along curved concave-upward surfaces or move as relatively intact planar sheets rather than tumbling or flowing, and creeps – the extremely slow, gradual, and continuous downslope movement of regolith over billions of years. On the Moon, elephant hide textures (EHT) and girlands are distinct mass wasting phenomena. EHT (Kreslavsky et al. 2023) consists of slow, widespread hummocky ripples triggered by seismic shaking. Although individual motions are small, the cumulative effect of seismic shaking over geologic time steadily lowers relief and infills small-scale depressions. Girlands (Kereszturi et al. 2022) are localized, rapid granular debris flows with distinct lobate margins that occur on steeper slopes.

Paracelsus C is thought to date back to the pre-Nectarian period between ~4.5 to ~3.9 billion years ago when the lunar crust was formed. This is the period before the formation of major basins, including the Nectaris Basin. The southern interior wall of Paracelsus C rises ~3 km above the crater floor. The crater floor is generally smooth with hummocky terrain near the southern wall, interpreted as ancient mass wasting deposits. Grooves and debris cones indicate downslope transport in the past, though the absence of boulder trails or fresh exposures suggests that major slope failure is no longer active. The presence of EHT on the crater walls is consistent with slow regolith creep rather than recent landsliding.

The features of interest sit atop a hill near the southern floor of the crater at –21.64°, 165.08°. Regolith creep in the immediate vicinity of these features appears to follow the topography sloping down from east to west as indicated in Figure 3.

Data and Methods

Morphometric Analysis

A quantitative analysis of the size and shape of P1–P3 was performed to understand why they appear different than typical lunar features. Our analysis is based on three LROC images acquired in the lunar morning, midday, and afternoon (Figure 4) that were resampled to 0.55 m/pixel and coregistered to QuickMap terrain height and LOLA data at the same resolution (Figure 5). Based on the afternoon image, P1 is ~58 m long. The width cannot be measured in this image because the southern side is shadowed. With less shadow in the higher sun angle morning image, the width appears to be ~23 m. Length and width measured in midday image were ~64 m and ~18 m, respectively, yielding an estimated length and width of 61 ± 3 m by × 20.5 ± 2.5 m for P1. P2 is self-shadowed in the morning image and cannot be fully delineated in the lower contrast midday image. Based on just the afternoon image it is ~44 m long and ~22 m wide.

Since the terrain surrounding these features is not flat, estimation of height from shadow length is problematic. LROC NAC Digital Terrain Models (DTM) have resolutions 2–5 m with a vertical accuracy < 1 m and absolute horizontal accuracy within 10 m (Henriksen et al. 2015). QuickMap NAC-DTM terrain height transects along the length of P1 and P2 indicate maximum heights above the surrounding terrain of 10.4 m and 10.2 m, respectively (Figure 6).

P3 shows two visible sides. Measurements of the north and west sides in the afternoon image are ~5.5 m and ~9.5 m. The feature is not well resolved in the other two images. The measured angle between the two sides is ~110°. Shadows west and east of P3 in the morning and afternoon images are consistent with QuickMap terrain height transects indicating a peak in the topography from south to north and a falloff from east to west (Figure 7). The estimated height above the terrain north and south is ~1.8 m. The falloff west of the feature is ~2.3 m over a distance of ~10.45 m, which corresponds to slope of ~12.4°. This value is 2.4° lower than the average LOLA slope of 14.8° estimated over the same area, which has a slope uncertainty between 1.5° and 2.5° (Smith et al. 2011).

An analysis of the steepest slopes on the Moon finds slopes significantly greater than the angle of repose (~35°) are rare due to the limited cohesion/strength of fractured and fragmented regolith of the lunar highlands, and the absence of processes producing steep slopes in the recent geological past (Kreslavsky and Head 2016). LOLA slopes within a 1 km radius of the features of interest were analyzed. A peak value of 64.4° was measured over P1. Closer examination reveals the peak value is actually due to LRO-DTM processing artifacts that can be seen in the QuickMap terrain height data (Figure 5). Slopes along the lengthwise terrain height transects plotted in Figure 6 are shown in Figure 8. The transect along P1 is just above the artifacts noted above. LOLA slopes are consistently higher than slopes computed from QuickMap terrain height (TH). Average LOLA and TH derived slopes along P1 and P2 transects are $32.3 \pm 10.5°$ and $12.2 \pm 7.8°$, and $22.6 \pm 12.4°$ and $12.8 \pm 11.7°$, respectively. Peak values of LOLA and TH derived slopes along P1 and P2 are 51.8° and 42.5°, and 50.4° and 45°. 37% of LOLA slope pixels along the P1 transect exceed 35°. 20% of LOLA slope pixels along the P2 transect exceed 35°.

Visual Interpretation

In order to better understand the morphology of P1–P3, synthetic images were generated by texture mapping the morning, midday, and afternoon LROC images (Figure 4) onto terrain height maps to produce a series of synthetic views from different look angles. Due to the presence of LRO-DTM processing artifacts in the QuickMap terrain height data, a height map computed from the LROC images using shape from shading (SFS), which is described in the appendix, was used instead.

Figure 9 (left) shows the upslope ends of P1 and P2 looking west. Based on the morning and midday images, the northeast end (a) and southeast side (d) of P1 appears to be exposed above the surrounding regolith. The textured appearance of the southeast side in the midday image suggests that P1 could be bare rock (e.g., an ejecta block, a boulder, or exposed bedrock). Figure 9 (right) shows the downslope ends of P1 and P2 looking east. Lacking this texture, the southwest end (b) and northwest side (c) of P1 in the afternoon image could be covered by regolith.

The high sun angle midday image reveals subtle textures not evident in either the morning or afternoon images. Contrast enhancement of the morning image shows a striated or stratified texture running along the top of P2 (f) similar to the southeast side of P1. In the morning image, much of P2 is self-shadowed (top left). Irregularities along the shadow edge having a corrugated appearance appear to coincide with the texture (f) noted above.

Figure 10 (left) indicates the corrugations along the shadow edge of P2 in the morning image may be related to the textured pattern (f) seen in the midday image. P2 also contains several small circular pits along the top (e), a structure resembling a short linear rille or graben (g) along its south side, and a small impact crater (h).

Compositional Analysis

A preliminary analysis of the composition of P1 and P2 and their surrounding area was performed using global map products derived from the Kaguya multiband imager (Lemelin et al. 2016) available within QuickMap. These products do not resolve P1-P3 individually and therefore provide only regional compositional context.

Where the nearside contains dark regions known as maria and lighter colored highlands, the farside is almost all highlands. Plagioclase, which is a major mineral found in both the Earth's and the Moon's crust, is contained in highland material. Highland material tends to be lower in iron oxide (FeO) than maria. As shown in Figure 11, there is an inverse relationship between Kayuga FeO (a) and plagioclase (b) abundance (wt%) over this area in Paracelsus C. Small craters north and east of the features of interest show up as lower FeO (5 wt%), which is consistent with them having excavated fresh plagioclase-rich material from beneath the surface. The depression to the west has a higher FeO (9.8 wt%) consistent with being highland type material that has undergone space weathering and is therefore not as fresh as that surrounding the small craters. The region containing the features also has a relatively high FeO (8.5 wt%) indicating a greater degree of space weathering than the immediate surroundings.

The amount of orthopyroxene (c), which acts as a marker for deeper, more primitive, or lower-crustal material tends to be inversely related to the amount of clinopyroxene (d), which is typically associated with later-stage igneous differentiation, mare volcanism, or melt sheets. Orthopyroxene abundance appears to be slightly higher around P1 and P2 (8–10 wt%) compared to the surrounding terrain (0–6 wt%).

The derived Optical Maturity (OMAT) (f) shows small craters north of the features of interest as having higher OMAT values (0.17–0.19) consistent with optically more immature (fresher) material compared to the area around the features with lower OMAT values (0.13–0.14) indicating a longer exposure to space weathering.

Given their limited (512 pixels/degree) resolution, the QuickMap compositional layers are not ideal for small-scale features. The olivine layer (e) indicates a significant increase in olivine abundance in the vicinity of P2 (17.1 wt%) compared to the surrounding area (0–9.5 wt%), though the spatial resolution limits precise attribution to the feature itself. Olivine is otherwise quite scarce over the surrounding area (Sun and Lucey 2024) with the nearest concentrations at Aitken crater (Yamamoto et al. 2010) approximately 260 km to the northeast (Figure 12).

Results

To what extent do P1-P3 resemble better known and understood lunar features? Figure 13 presents some examples:

A. Section of exposed bedrock along the edges of Hadley Rille, near Apollo 15 landing site (Sato 2011). Portion of NAC image M113941548L is 500 m wide.
B. Boulders on the top of the central uplift in Anaxagoras Crater (Bray 2010). The surface beneath these boulders contains large blocks, most likely fractured bedrock outcrops. Portion of NAC image M122273232RE is 425 m wide.
C. High albedo rock exposures within a volcanic vent in the Schrödinger impact basin (Kring et al. 2025). LROC basemap ~2 km wide (75.35° S, 139.48° E).
D. Large boulder (~ 120 m across) within impact melt pond on the central peak of Tycho (Barry 2011). (NAC image M127008391L)
E. Stratified ejecta block (~ 80 m long) near an unnamed fresh crater on the farside (13.13° N, 127.61° E) (Alanis 2011). (NAC image M110757216R)
F. Boulder (~10 m across) in ejecta zone of crater near the center of Paracelsus C. NAC image M118769870L.
G. Boulder trail and boulder fragment (Plescia 2013). Portion of M134991788 is 400 m wide. Apollo image AS17-140-21496 of astronaut Jack Schmitt at Station 6 near boulder fragment (Zastrow 2022).

Where one side of P1 appears textured and the other side smooth in the midday image, P2 appears smooth on both sides. A texture not unlike that on the southeast side of P1 appears to run along the spine of P2 suggesting the possibility that these two features share a common origin. End to end, P2 and P3 are approximately the same length as P1 (Figure 14). While P3 could be an isolated boulder, it is also possible that all three features could be related. Bedrock exposures generally occur over extended areas such as along ridges (A), within crater floors (B), and the sides of volcanic vents (C). P1–P3 appear to be unique with no other similar features nearby.

In examining the morphology, distribution, and preservation of large boulders on the Moon, while large blocks (>50–100 m) can remain intact for tens to hundreds of millions of years, they eventually begin to exhibit characteristic signs of erosion (Basilevsky et al. 2013, Basilevsky et al. 2015). Erosional processes span a range from gradual micrometeorite abrasion ("sandblasting") to catastrophic fragmentation caused by single high-energy events. Larger rocks are more likely to be affected due to their greater cross-sectional area and, potentially, a higher density of internal structural flaws. Thermal stresses also contribute to rock breakdown (Molaro et al. 2017). A large boulder perched on an impact melt pond in a depression on the summit of Tycho's central peak (D) is thought to be as old as the crater itself, ~108 million years old. Having survived for so long, it is not entirely intact. A halo of smaller rocks beneath its more vertical sides are evident, likely having spalled off the main block following sub-critical impacts and thermal cycling. The lack of spallation debris/fractures typically seen in lunar boulders that have been subject to long periods of space weathering appear absent around P1 and P2.

The striated texture on the southeast side of P1 and along the top of P2 resembles the layered texture of stratified ejecta blocks (E). P1 could be a horizontally layered block covered by regolith at the southwest end and northwest side. P2 could be a vertically layered block with regolith accumulations on all sides.

There are two small pits (e) identified in Figure 10 at the eastern end of P2 along this texture. Figure 15 shows these plus two other small pits near the other end that appear to correspond with the corrugations seen in the afternoon image. If these pits are impact craters, the absence of fracturing may reflect resolution limits or the effect of "regolith blanketing" where a thick layer of regolith is able to dissipate the kinetic energy of hypervelocity impacts (Schonberg et al. 2010). While regolith covering the low slope areas of P2 could explain the relative lack of damage to (g) by an impact (h), it is challenged to account for the lack of visible damage around the four pits along the high slope spine of P2 which likely lacks the same covering.

Other smaller blocks in Paracelsus C (F) are morphologically distinct from P1-P3. For comparison (G) shows one of five boulder fragments that lie at the end of a 980 m long boulder trail 10-12 m wide that formed as a single large boulder rolled down the hill. The exposure duration of this boulder is ~17–21 My (Watters and Schmerr 2025). There is no evidence of boulder tracks leading to P1–P3, implying that if they did roll down from the crater rim, they must be old enough for space weathering to have substantially smoothed their tracks.

The cumulative effects of space weathering can collectively be modeled as topographic diffusion (O'Brien and Byrne 2021):

$$\frac{\partial z}{\partial t} = \kappa\left[\frac{\partial^2 z}{\partial x^2} + \frac{\partial^2 z}{\partial y^2}\right]$$

where z is the height (topography) that is diffusing in space and over time. The above process can be simulated on a grid by the finite difference equation (Hill 2026):

$$z_{ij}^{n+1} = z_{ij}^{n} + \kappa\Delta t\left[\frac{z_{i+1,j}^{n} - 2z_{ij}^{n} + z_{i-1,j}^{n}}{(\Delta x)^2} + \frac{z_{i,j+1}^{n} - 2z_{ij}^{n} + z_{i,j-1}^{n}}{(\Delta y)^2}\right]$$

where Δx and Δy are the grid spacing (row and column pixel resolution), Δt is the time interval, and κ is the diffusion coefficient. The maximum time interval that we can allow without the above equation becoming unstable is

$$\Delta t = \frac{1}{2\kappa}\frac{(\Delta x\Delta y)^2}{(\Delta x)^2 + (\Delta y)^2}$$

O'Brien and Byrne (2021) determined that the diffusivity needed to match the observed roughness of the lunar maria is 0.109 m^2/My. Studies on the effect of topographic degradation on small lunar craters indicate the diffusivities of the maria and highlands are roughly the same (Yang et al. 2021, Du et al. 2019).

Topographic diffusion was used to understand the persistence of the linear rille/graben structure at the base of P2 to space weathering. A height map over a rectangular area over P2 (Figure 16) containing this structure (~ 4.4 m wide) and a small crater (~ 5.5 m in diameter) was computed using shape from shading. The diffusion model simulated the effect of lunar impact gardening over this area over a period of 128 My using a mare/highlands diffusion coefficient of 0.109 m^2/My (Figure 17). A diffusion model with no boundaries is classically formulated as an initial value or Cauchy problem. By assuming an unbounded domain and letting boundaries recede to infinity, the spatial domain requires no boundary conditions. Instead, it relies only on the initial condition and the spatial decay (diffusion) constraint. Diffused heights plotted along the transect plot in Figure 16 indicate that a 4.4 m wide reconstructed topographic feature would be substantially smoothed after approximately 16 My under a linear diffusion model with κ = 0.109 m^2/My.

As noted in earlier in Figure 9, the north side of P1 appears to be covered by a "fillet" of regolith. Analysis and modeling of fillets by topographic diffusion (Rüsch and Wöhler 2022) have demonstrated that significant amounts of regolith can accumulate around blocks of comparable width and height to P1 over a timescale of ~50 My. The degree of regolith accumulation at the base of P2 is less clear. The adjacent impact seems to have had little effect on the rille/graben structure suggesting the possibility of a relatively thick apron of regolith blanketing around P2.

Using the same surface in Figure 16, we repeated our diffusion experiment increasing the horizontal and vertical scale factors by the same amount to simulate the effect of space weathering on a depression roughly the width of the Apollo 17 Station 6 boulder trail (Plescia 2013). Such a depression would disappear over a timescale of ~100 My. The survival time of trails that might have been produced by P1 and P2, which are considerably larger than the Station 6 boulder (~18 x 10 x 6 m), would be considerably longer.

Discussion

Table 2 summarizes our analysis of the three features in Paracelsus C. The following preliminary conclusions can be made based on initial morphometric/compositional analyses:

1) The slope angles of P1 and P2 exceed typical slopes observed in degraded highland terrains and suggest unusually well-preserved relief.
2) This is consistent with the presence of fine-scale details, specifically a short linear rille/graben-like structure along the southeast side of P2 ~4.4 m wide that would be substantially smoothed over a timescale of ~16 My under a linear diffusion model with $\kappa = 0.109\ m^2/My$.
3) High slope angles and fine scale details appear difficult to reconcile with low OMAT values that indicate a higher degree of space weathering in the immediate vicinity of P1 and P2 relative to the surrounding terrain.
4) This is supported by a greater FeO abundance near P1 and P2 relative to craters to the north indicating a greater degree of space weathering, both of which support long emplacement/exposure.
5) A significant accumulation of regolith on the northwest side and southwest end of P1 indicates an emplacement timescale of ~50 My. A similar apron of regolith may surround P2 as well.
6) Only one side of P1 appears to be covered in regolith. Slope angles greater than the angle of repose could explain at the apparent lack of regolith on the southeast side of P1; however, artifacts in both QuickMap NAC-DTM and LOLA data prevent comparison of slope angles of the two sides at this time.

The coexistence of apparent long-term regolith accumulation around P1 and preservation of meter-scale morphology on P2 presents a potential paradox. It is possible these features are composed of a harder material that is more resilient to space weathering, the rate of diffusion is lower, have only recently been exposed, or are shielded by the local topography.

Table 3 lists four possible origin hypotheses/mechanisms. There is no visible boulder trail associated with the features in Paracelsus C. Trails produced by boulders the size of the Apollo 17 Station 6 boulder, which is considerably smaller than P1 and P2, are estimated to persist over diffusion timescales >100 My which is considerably longer the emplacement time inferred from regolith fillets.

A relatively high level of olivine in the area around P2 relative to the surrounding terrain and high levels of olivine surrounding Aitken crater suggest a possible connection with the SP–A impact event. However, where the SP–A impact would likely have had enough energy, no recent impact events would have had sufficient energy to eject blocks the size of P1 and P2 hundreds of km.

The similarity in texture of the southeastern side of P1 and the top of P2 suggest a common origin, either ejecta from the same source, or exposed bedrock. While P3 appears to be an isolated feature, it is possible that all three features are megaregolith exposures. Underneath the regolith layer in the lunar highlands lies a layer of material ejected during the formation of the large basins (Wiggins et al. 2019). However, this layer is particularly thin in the SP–A impact basin (Besserer et al. 2014) and there are no other similar exposures in Paracelsus C. Bedrock exposures may be favored by the absence of transport indicators, alignment of P2 and P3 with P1, partial regolith mantling, and the possibility that SP–A ejecta or uplifted megaregolith materials are exposed along pre-existing structural weaknesses.

Impact melt remnants are a fourth possibility. Olivine-rich rocks on the farside are thought to have crystallized directly from the massive magma ocean generated by the SP–A impact. Chang'e-4 rover made in situ spectral measurements on materials containing olivine and orthopyroxene rich assemblages in almost equal fractions that could have originated from a differentiated SP–A impact melt pool (Gou 2020).

An impact-melt origin provides one possible explanation for the apparent preservation state of these features. Unlike the surrounding megaregolith, which is highly fragmented by billions of years of impact processing, impact-melt deposits can form relatively coherent lithologies. If the features contain more resistant material than the surrounding terrain, local degradation rates may differ from those assumed in simple diffusion models. This possibility could help reconcile the preservation of steep slopes and meter-scale morphological detail with evidence for prolonged surface exposure derived from OMAT and regolith accumulation.

Conclusion

Of the four possible emplacement/exposure mechanisms considered—downslope transport, ejecta block, bedrock exposure, and impact-melt remnant—none is clearly favored by the available data. The features in Paracelsus C appear distinct from the surrounding terrain in terms of size, shape, and regional compositional setting. The coexistence of steep slopes, preserved meter-scale morphology, mature surrounding surface materials, and evidence for regolith accumulation indicates an unusual preservation history relative to the surrounding crater floor suggesting the possibility P1–P3 may be more competent than other local features. The available imagery shows only much smaller nearby blocks and no close analogs to P1-P3 within Paracelsus C. Open questions regarding their morphology and fine-scale detail highlight the need for further study, including higher-resolution terrain and slope measurements, improved mineralogical characterization, and higher-resolution imaging of poorly resolved features such as P3 and the fine-scale structures observed on P2.

At present, the available data are sufficient to establish that P1–P3 are morphologically unusual relative to the surrounding terrain, but insufficient to uniquely determine their origin.

Declaration of generative AI and AI-assisted technologies in the manuscript preparation process

During the preparation of this work, the author used ChatGPT to assist in literature search and to cross-reference reviewers' comments with specific revisions made. The author reviewed and edited the output and takes full responsibility for the content of the published article.

References

Carlotto, Mark J., Ridge, Francis L., and Sirisena, Ananda L. (2016). Image Analysis of Unusual Structures on the Far Side of the Moon in the Crater Paracelsus C. *Journal of Space Exploration*, Vol. 4, Issue 3.

Carlotto, Mark (2026). A biologically inspired target screener for lunar surface anomaly detection. *Proc. SPIE 14049, Signal Processing, Sensor/Information Fusion, and Target Recognition XXXV*, https://doi.org/10.1117/12.3114403

Kelahan, Cameron, Angerhausen, Daniel, Lesnikowski, Adam, Bickel, Valentin (2025). Lunar Surface Anomaly and Technosignature Detection with Unsupervised Machine Learning Analysis of Lunar Reconnaissance Orbiter Images. *246th Meeting of the American Astronomical Society, Bulletin of the American Astronomical Society*, Vol. 57, No. 4.

Xiao, Zhiyong, Zeng, Zuoxun, Ding, Ning, and Molaro, Jamie (2013). Mass wasting features on the Moon – how active is the lunar surface? *Earth and Planetary Science Letters*, 376, 1-11, https://doi.org/10.1016/j.epsl.2013.06.015.

Kreslavsky, M, Zubarev, A., Nadezhdina, I., and Bondarenko, N (2023). Non-diffusive regolith transport on the Moon. *54th Lunar and Planetary Science Conference* (LPI Contrib. No. 2806).

Kereszturi, A., Tomka, R., Gläser, P. A., Pal, B. D., Steinmann, V., & Warren, T. (2022). Characteristics of de Gerlache crater, site of girlands and slope exposed ice in a lunar polar depression. *Icarus*, 388, 115231.

Henriksen, M. R., Manheim, M. R., Speyerer, E. J., Boyd, A. K., & Robinson, M. S. (2015). LROC NAC DTM Production. *Second Planetary Data Workshop* (Abstract #7010).

Smith, D. E., Zuber, M. T., Neumann, G. A., Mazarico, E., Head, J. W., Torrence, M. H., & LOLA Science Team. (2011). *Results from the Lunar Orbiter Laser Altimeter (LOLA): Global, high-resolution topographic mapping of the Moon*. 42nd Lunar and Planetary Science Conference.

Kreslavsky, M. A. and Head, J. W. (2016). The steepest slopes on the Moon from Lunar Orbiter Laser Altimeter (LOLA) data: Spatial distribution and correlation with geologic features. *Icarus*, 273, 329–336. https://doi.org/10.1016/j.icarus.2016.02.036

Sato, Hiroyuki (2011). Layers near Apollo 15 landing site. NASA/GSFC/Arizona State University. https://lroc.im-ldi.com/images/355

Bray, Veronica (2010). Exposed Fractured Bedrock in the Central Peak of the Anaxagoras Crater. NASA/GSFC/Arizona State University. https://lroc.im-ldi.com/images/155

Kring, D. A., Bickel, V. T., Lee, P., Fagan, A. L., Heldmann, J. L., Elphic, R. C., Lawrence, D. J., Parker, T. J., & Schmitt, H. H. (2025). Potential bedrock exposures of Schrödinger impact melt sheet and/or polymict impact breccias within a crater floor fracture system and volcanic vent. *Planetary and Space Science*, 257, 106063.

Barry, Caela (2011). Tycho Crater's Central Peak on the Moon. NASA Goddard/Arizona State University. https://science.nasa.gov/resource/tycho-craters-central-peak-on-the-moon/

Alanis, Rafael (2011). Stratified Ejecta Blocks. NASA/GSFC/Arizona State University. https://science.nasa.gov/photojournal/stratified-ejecta-blocks/

Plescia, Jeff (2013). Station 6 – Apollo 17. NASA/GSFC/Arizona State University. https://lroc.im-ldi.com/images/759

Zastrow, Mark (2022). Apollo 17: Humanity's last trip to the Moon. *Astronomy*. https://www.astronomy.com/space-exploration/apollo-17-humanitys-last-trip-to-the-moon/

Basilevsky, A.T., Head, J.W., and Horz, F. (2013) Survival times of meter-sized boulders on the surface of the Moon. *Planetary and Space Science*. Vol. 89 pp.118–126

Basilevsky, A.T., Head, J.W., Horz, F. and Ramsley, K.R. (2015) Survival Times of Meter-Sized Rock Boulders on the Surface of Airless Bodies. *Planetary and Space Science*. Vol. 117, pp 312-328.

Molaro, J.L., Byrne, S. and Le, J-L (2017) Thermally induced stresses in boulders on airless body surfaces, and implications for rock breakdown. *Icarus*, Vol. 294, pp 247-261.

Schonberg, W. P., Schäfer, F., & Putzar, R. (2010). Some comments on the protection of lunar habitats against damage from meteoroid impacts. *Journal of Aerospace En*gineering, 23(1), 90-97.

Watters, Thomas R. and Schmerr, Nicholas C. (2025) Paleoseismic activity in the moon's Taurus-Littrow valley inferred from boulder falls and landslides. *Sci. Adv*. 11, https://www.science.org/doi/10.1126/sciadv.adu3201

Lemelin, M., P. G. Lucey, L.R. Gaddis, T. Hare, and M. Ohtake (2016). Global map products from the Kaguya Multiband Imager at 512 ppd: Minerals, FeO and OMAT, *47th LPSC*, abs. #2994. http://www.hou.usra.edu/meetings/lpsc2016/pdf/2994.pdf

Sun, L., & Lucey, P. G. (2024). Lunar mantle composition and timing of overturn indicated by Mg# and mineralogy distributions across the South Pole-Aitken basin. *Earth and Planetary Science Letters*, 643, 118931

Yamamoto, S., Nakamura, R., Matsunaga, T. et al. (2010). Possible mantle origin of olivine around lunar impact basins detected by SELENE. *Nature Geoscience*, 3, 533–536.

O'Brien, P., and Byrne, S. (2021). Physical and chemical evolution of lunar mare regolith. *Journal of Geophysical Research: Planets*, 126, e2020JE006634. https://doi.org/10.1029/2020JE006634

Hill, Christian (2026) The two-dimensional diffusion equation. *Learning Scientific Programming with Python*. https://scipython.com/books/book2/chapter-7-matplotlib/examples/the-two-dimensional-diffusion-equation/

Yang, X., Fa, W., Du, J., Xie, M., & Liu, T. (2021). Effect of topographic degradation on small lunar craters: Implications for regolith thickness estimation. *Geophysical Research Letters*, 48(21), e2021GL095537.

Du, J., Fa, W., Wieczorek, M. A., Xie, M., Cai, Y., & Zhu, M.-H. (2019). Thickness of lunar mare basalts: New results based on modeling the degradation of partially buried craters. *Journal of Geophysical Research: Planets*, *124*(9), 2430–2459.

Rüsch, O., & Wöhler, C. (2022). Degradation of rocks on the Moon: Insights on abrasion from topographic diffusion, LRO/NAC and Apollo images. *Icarus*, *384*, 115088.

Wiggins, S. E., Johnson, B. C., Bowling, T. J., Melosh, H. J., & Silber, E. A. (2019). Impact fragmentation and the development of the deep lunar megaregolith. *Journal of Geophysical Research: Planets*, 124, 941–957. https://doi.org/10.1029/2018JE005757

Besserer, J., Nimmo, F., Wieczorek, M. A., Weber, R. C., Kiefer, W. S., McGovern, P. J., Andrews-Hanna, J. C., Smith, D. E., & Zuber, M. T. (2014). GRAIL gravity constraints on the vertical and lateral density structure of the lunar crust. *Geophysical Research Letters*, 41(16), 5771–5777.

Gou, S., Di, K., Yue, Z., Liu, Z., He, Z., Xu, R., Liu, B., Peng, M., Wan, W., Wang, Y., & Liu, J. (2020). Forsteritic olivine and magnesium-rich orthopyroxene materials measured by Chang'e-4 rover. *Icarus*, 345, 113776

Horn, B. K. P. and Brooks, M. J. (1986). The variational approach to shape from shading. Computer Vision, Graphics, and Image Processing 33(2), 174–208. DOI: 10.1016/0734-189X(86)90114-3

Hapke, B. W. (1963). "A theoretical photometric function for the lunar surface." *Journal of Geophysical Researc*h, 68(15), 4571–4586.

Horn, B.K.P. (1990) Height and gradient from shading. *International Journal Computer Vision*, 5, 37–75. https://doi.org/10.1007/BF00056771

Table 1 Image collection parameters. Solar azimuth angles computed from sub-spacecraft and sub-solar latitudes and longitudes.

Image	**Morning**	**Midday**	**Afternoon**
Product	M1168450258L[1]	M1237871462R[2]	M118769870L[3]
Orbit number	24067	33914	2636
Resolution	0.9 m/pixel	0.96 m/pixel	0.55 m/pixel
Emission angle	1.73°	1.16°	1.69°
Incidence angle	54.6°	31.6°	68.9°
Solar azimuth	66.5	-43.5	-71.6

Table 2 Summary of morphometric analysis.

	P1	**P2**	**P3**
Dimensions	$61 \times 20.5 \times 10.4$ m	$44 \times 22 \times 10.2$ m	$5.5 \times 9.5 \times 1.8$ m
LOLA peak slope	51.8°	50.4°	N/A
LOLA mean slope	32.3°	22.6°	14.8°
Terrain height peak slope	42.5°	45°	N/A
Terrain height mean slope	12.2°,	12.8°	12.4°
Characteristic diffusion smoothing timescale	~50 My	<16 My	N/A
Unresolved questions	Absence of fillet along southeast side. High slopes	Origin of rille/graben structure and circular pits along spine. High slopes	Extent of regolith covering/true shape

[1] https://data.lroc.im-ldi.com/lroc/view_lroc/LRO-L-LROC-3-CDR-V1.0/M1168450258LC
[2] https://data.lroc.im-ldi.com/lroc/view_lroc/LRO-L-LROC-3-CDR-V1.0/M1237871462RC
[3] https://data.lroc.im-ldi.com/lroc/view_lroc/LRO-L-LROC-3-CDR-V1.0/M118769870LC

Table 3 Origin hypotheses/mechanisms

Hypothesis/Mechanism	Supporting Evidence	Conflicting Evidence	Testable Prediction
Downslope transport	Crater-wall relief	No preserved tracks	Buried trail detectable
Ejecta block	Texture suggests a stratified eject block Size and shape consistent with an eject block	Isolated occurrence. No other nearby blocks.	Internal layering present in higher-resolution imagery
Bedrock exposure	No transport evidence	Isolated occurrence. No other nearby exposures	Continuity with subsurface structures
Impact melt remnant	Composition consistent with differentiated SP–A melt pools	Isolated occurrence. No other nearby concentrations	Melt-like composition

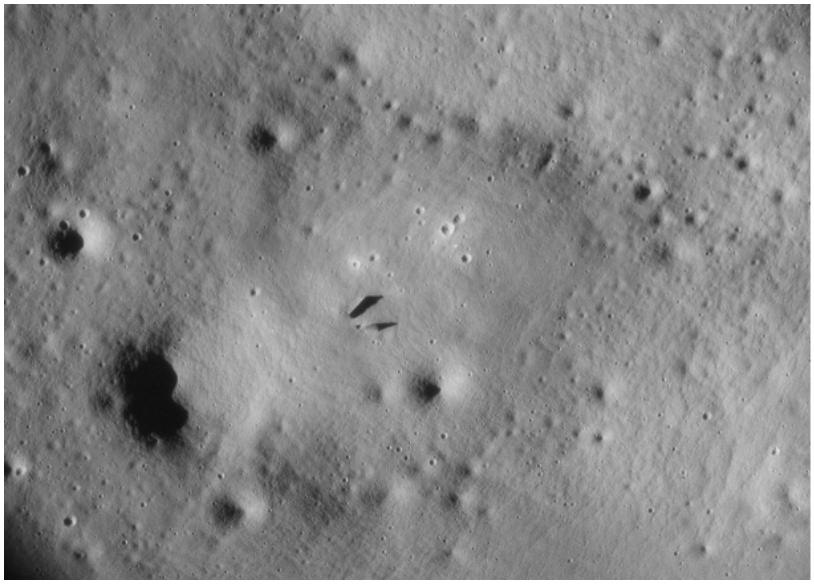

Figure 1 Historical photo showing portion of Apollo 15 panoramic image AS15-P-8868[4] containing objects of interest. The view is rotated with north up.

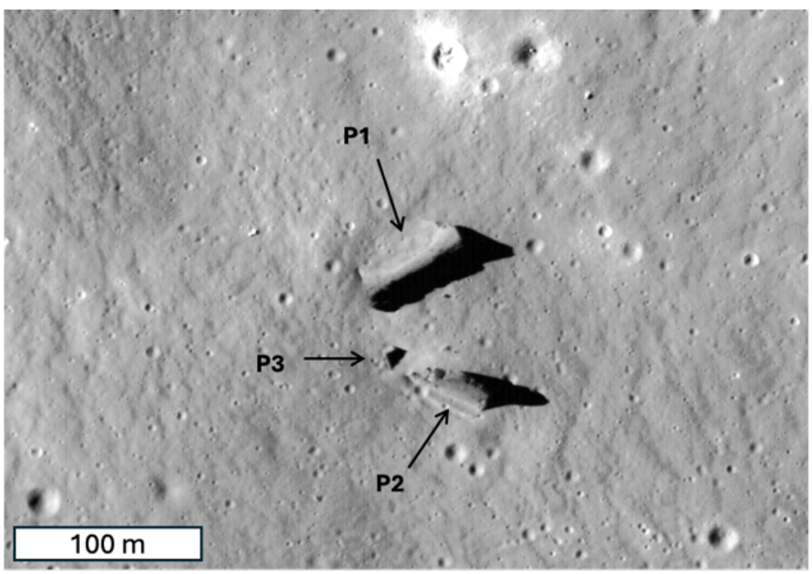

Figure 2 Features P1–P3 in LROC afternoon image M118769870L. Sun and sensor look angles are similar to AS15-P-8868. Image area ~430 x 310 m.

[4] https://data.lroc.im-ldi.com/apollo/view?camera=P&image_name=AS15-P-8868

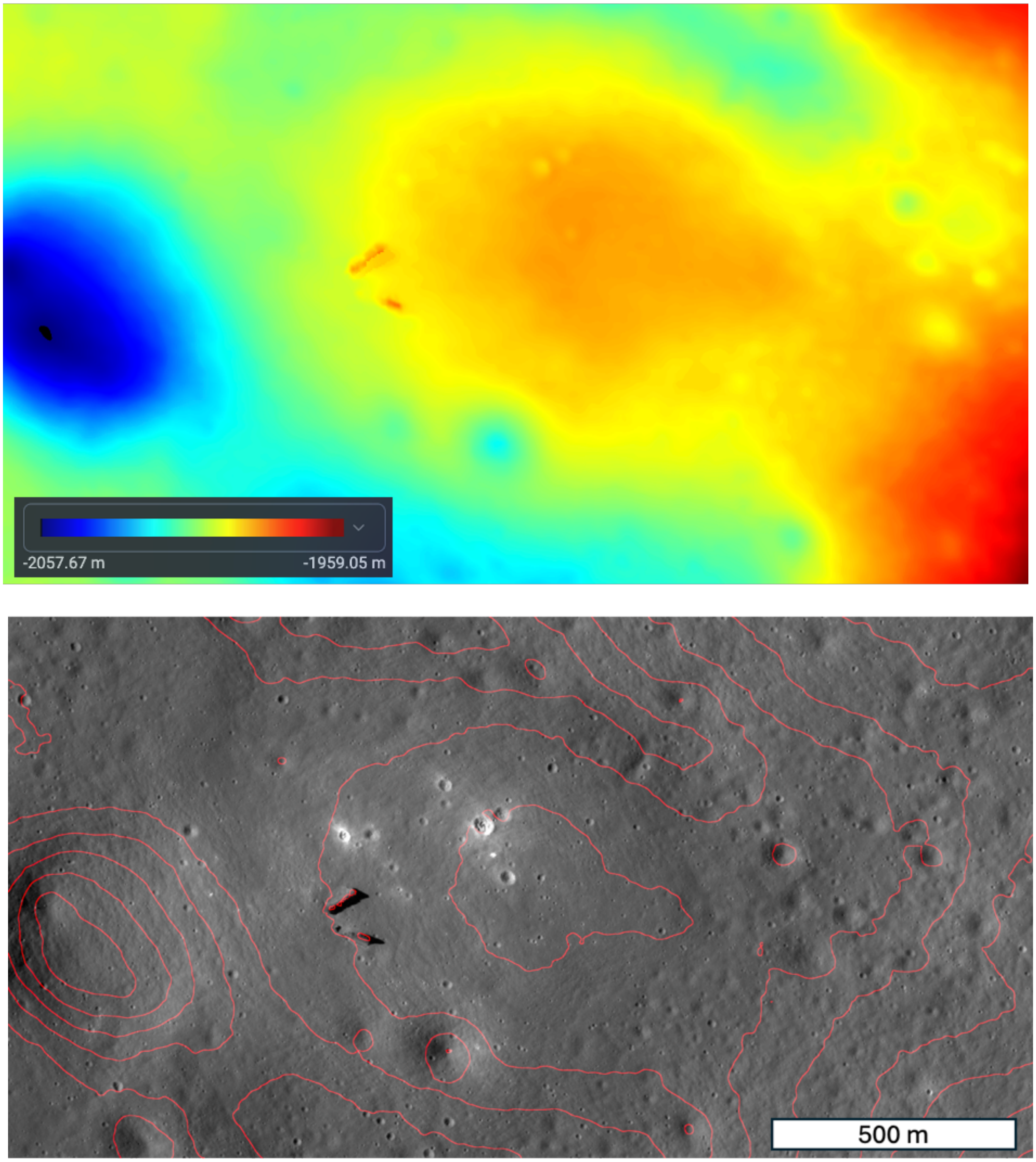

Figure 3 QuickMap terrain height map over region of interest (top). Image area ~2.1 x 1.3 km. Direction of regolith creep in the immediate vicinity of the features is from a hill to the east into a depression to the west (bottom). Contour interval is 10 m.

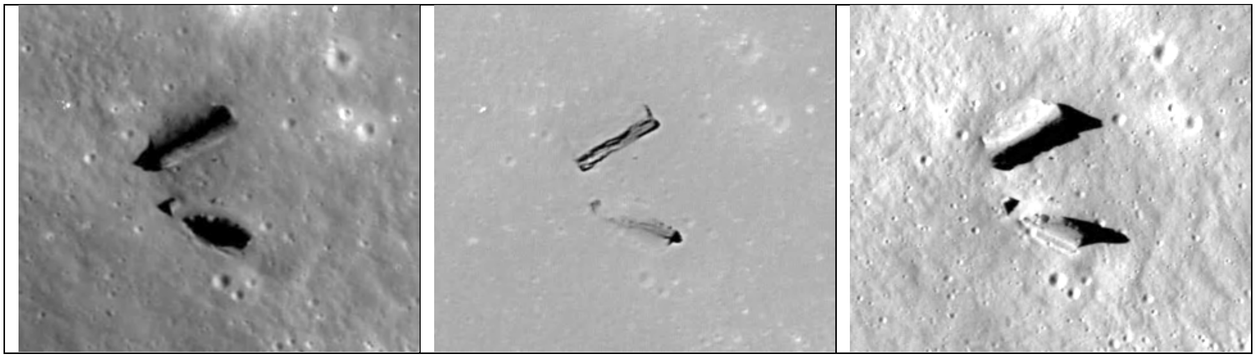

Figure 4 Co-registered LROC images: morning (left), contrast enhanced midday (middle), and afternoon (right). Same scale as Figure 2. Image area ~312 x 270 m.

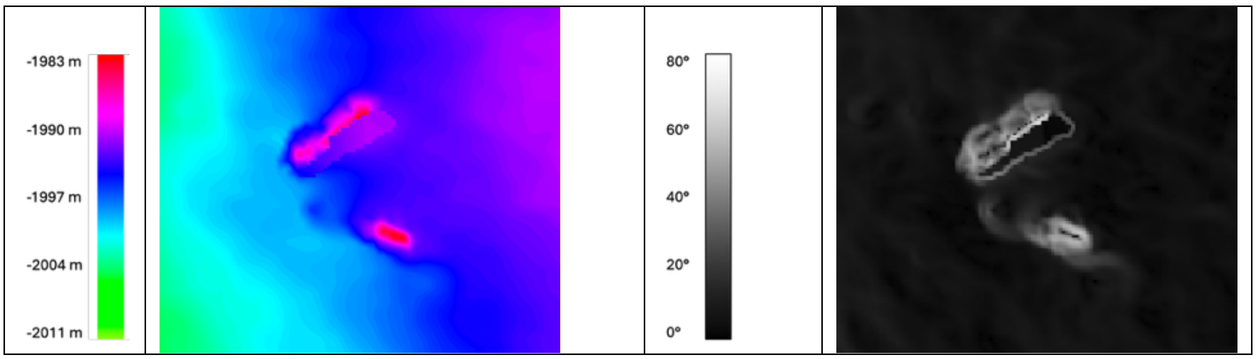

Figure 5 Co-registered QuickMap terrain height (left) and LOLA slope (right).

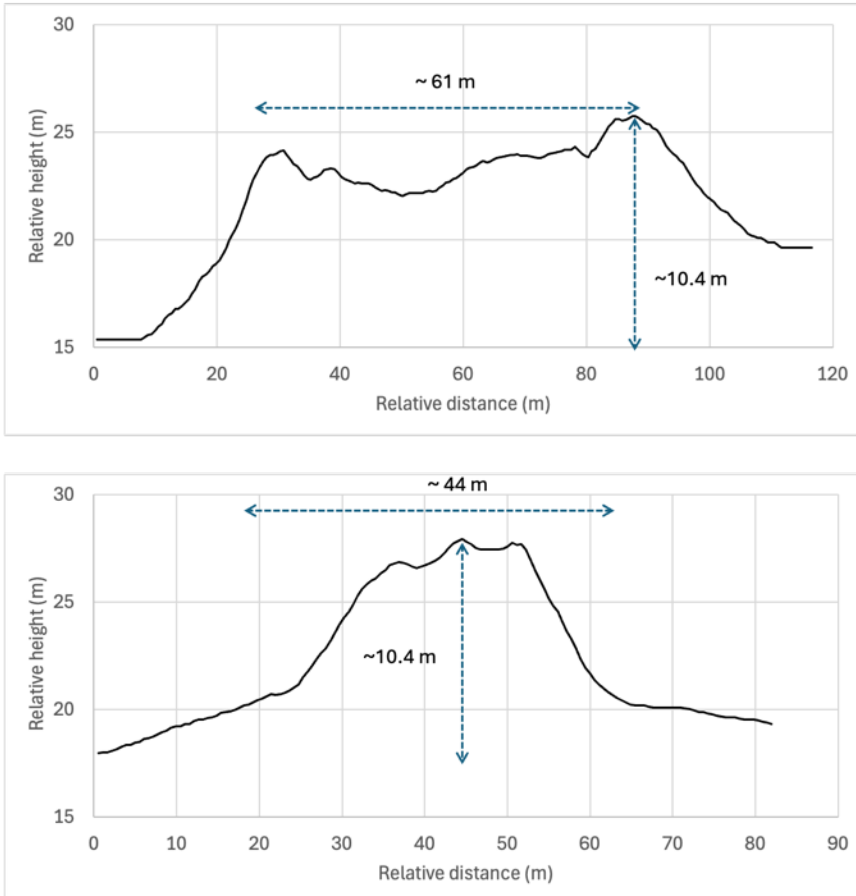

Figure 6 QuickMap height for transects lengthwise along P1 (top) and P2 (bottom). Transects shown in Figure 7. Indicated widths are LROC image measurements. Height uncertainty is < 1 m.

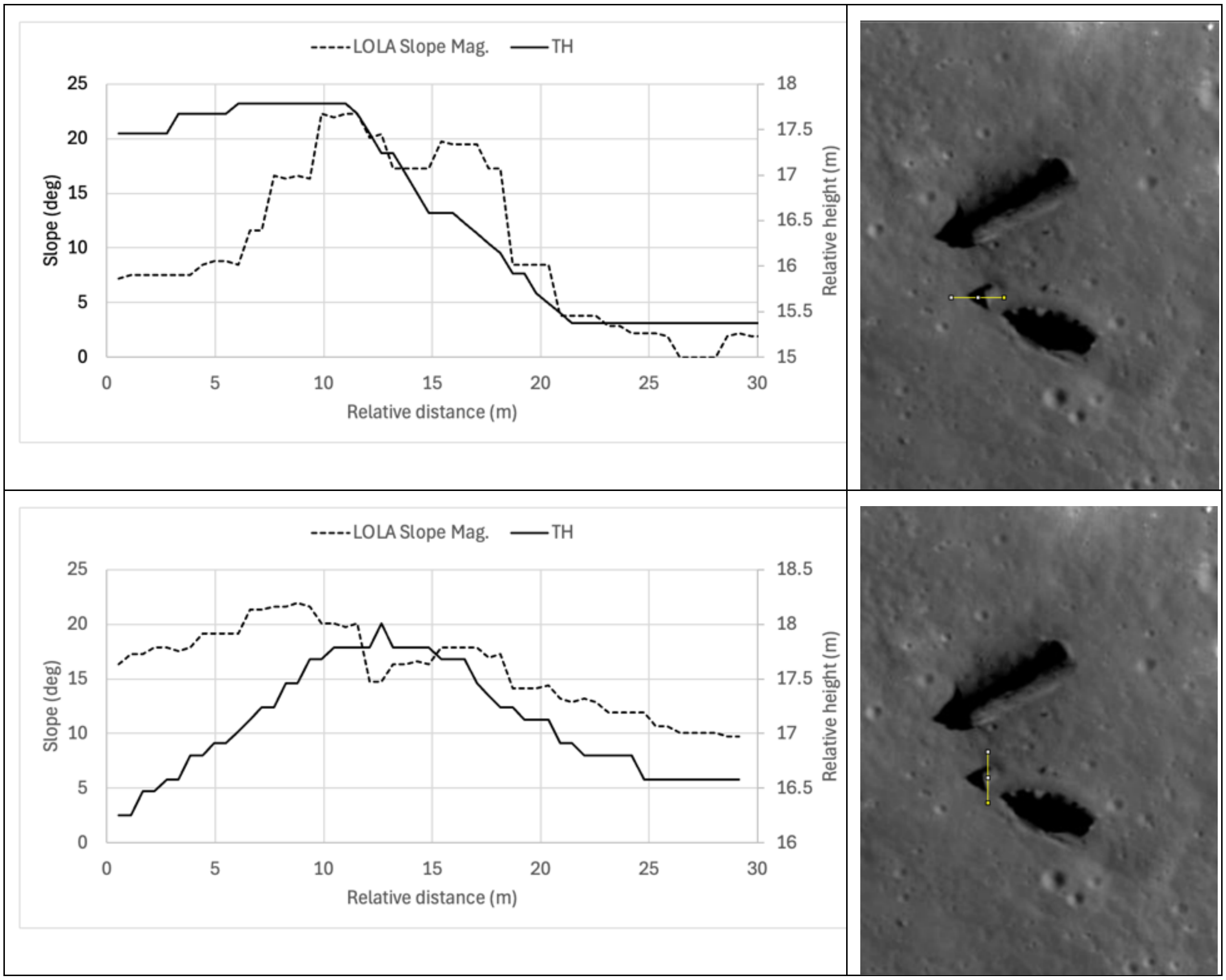

Figure 7 QuickMap terrain height for transects through P3 east to west (top) and south to north (bottom). Corresponding QuickMap LOLA slope magnitudes plotted on the secondary axis. LOLA slope uncertainty 1.5–2.5°.

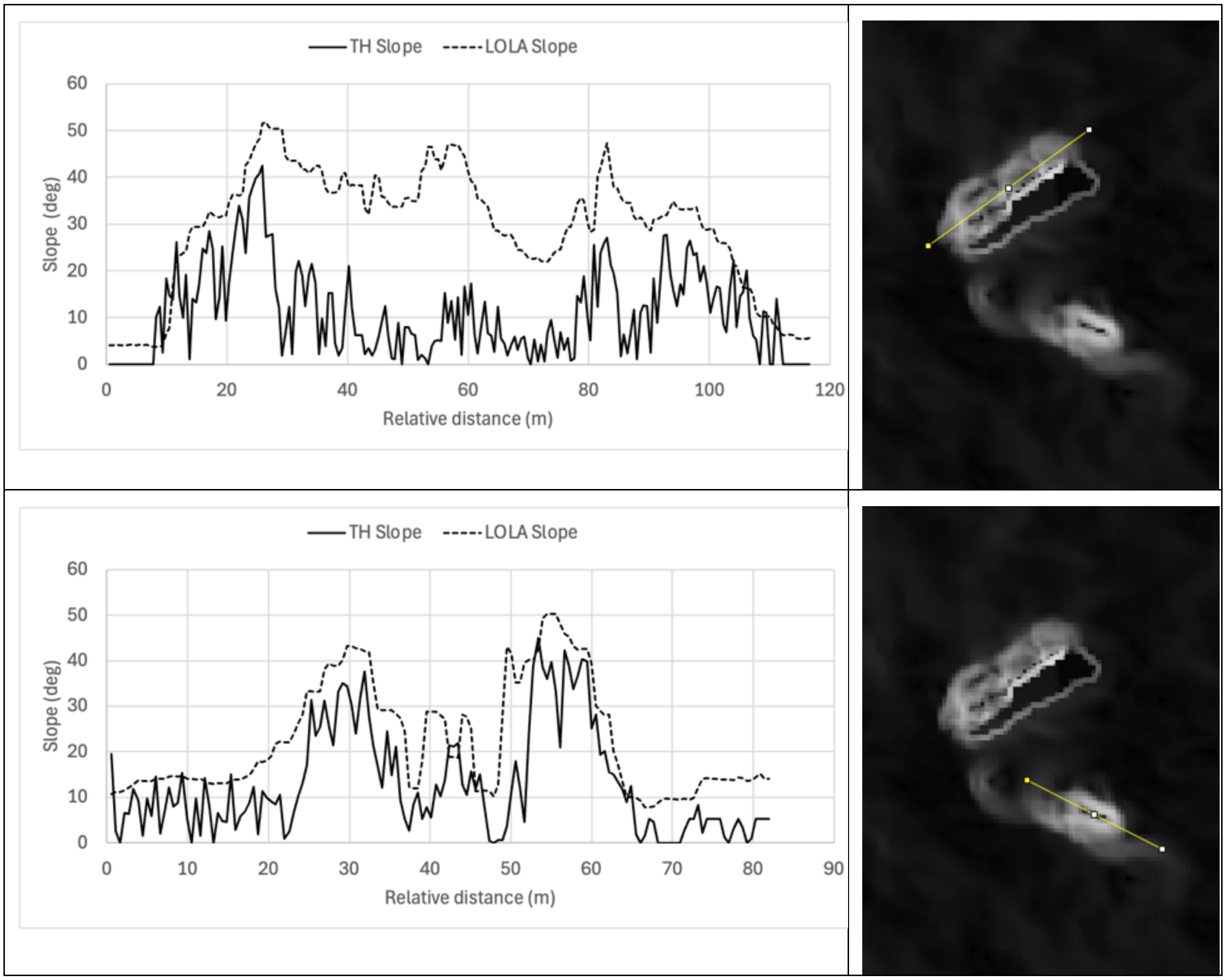

Figure 8 LOLA and terrain height derived slopes (left) for transects (right) along P1 (top) and P2 (bottom). LOLA slope uncertainty 1.5–2.5°.

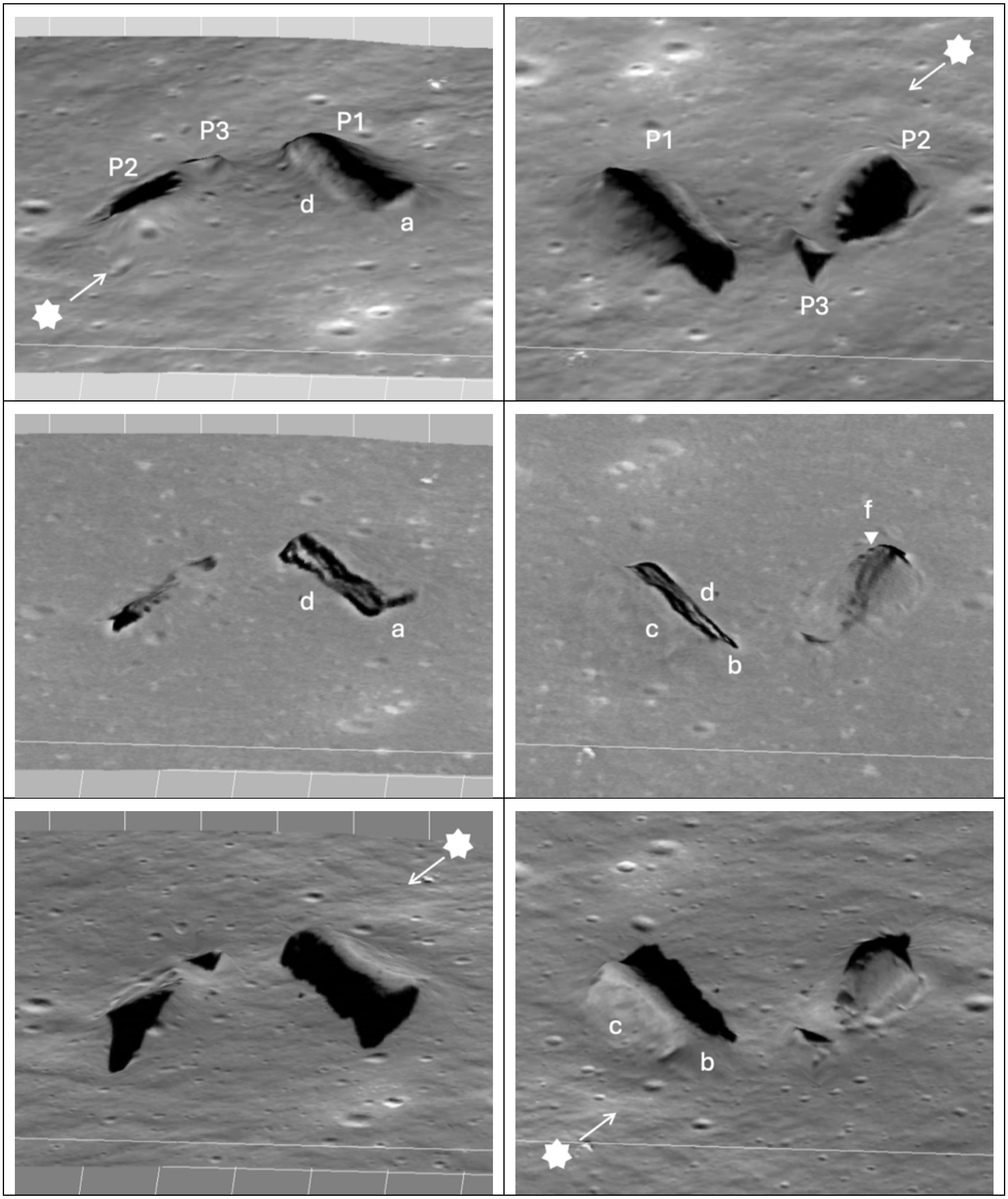

Figure 9 *Synthetic perspective views looking west of the morning (top left), contrast enhanced midday (middle left), and afternoon (bottom left) LROC images, and looking east of the morning (top right), midday (middle right), and afternoon (bottom right) LROC images. The views are oblique projections of the LROC images texture mapped over the fused QuickMap/SFS height map. Vertical exaggeration ~1.6.*

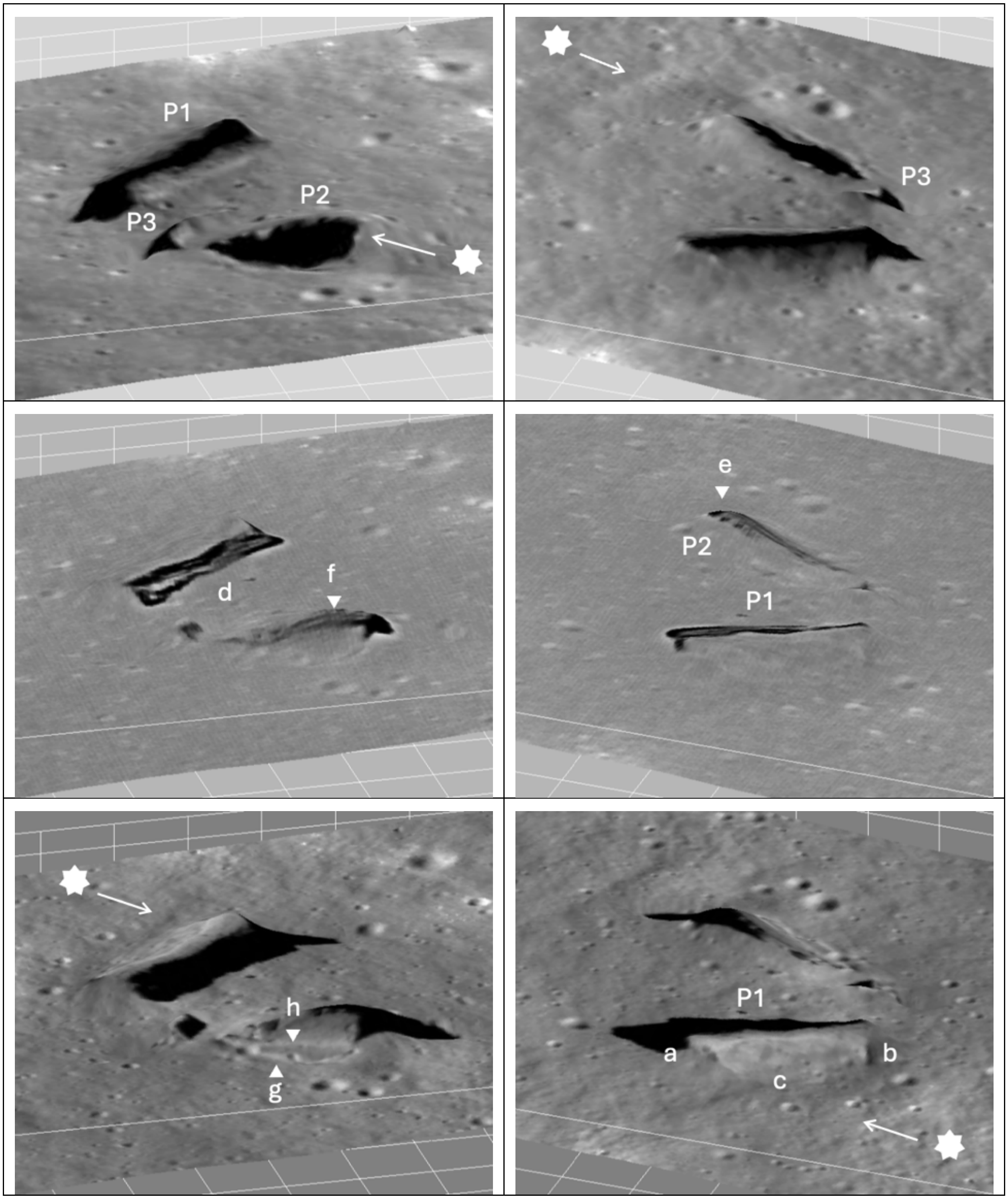

Figure 10 Synthetic perspective views looking north of the morning (top left), contrast enhanced midday (middle left), and afternoon (bottom left) LROC images, and looking south of the morning (top right), midday (middle right), and afternoon (bottom right) LROC images. As in the previous figure, the views are oblique projections of the LROC images texture mapped over the fused QuickMap/SFS height map. Vertical exaggeration ~1.6.

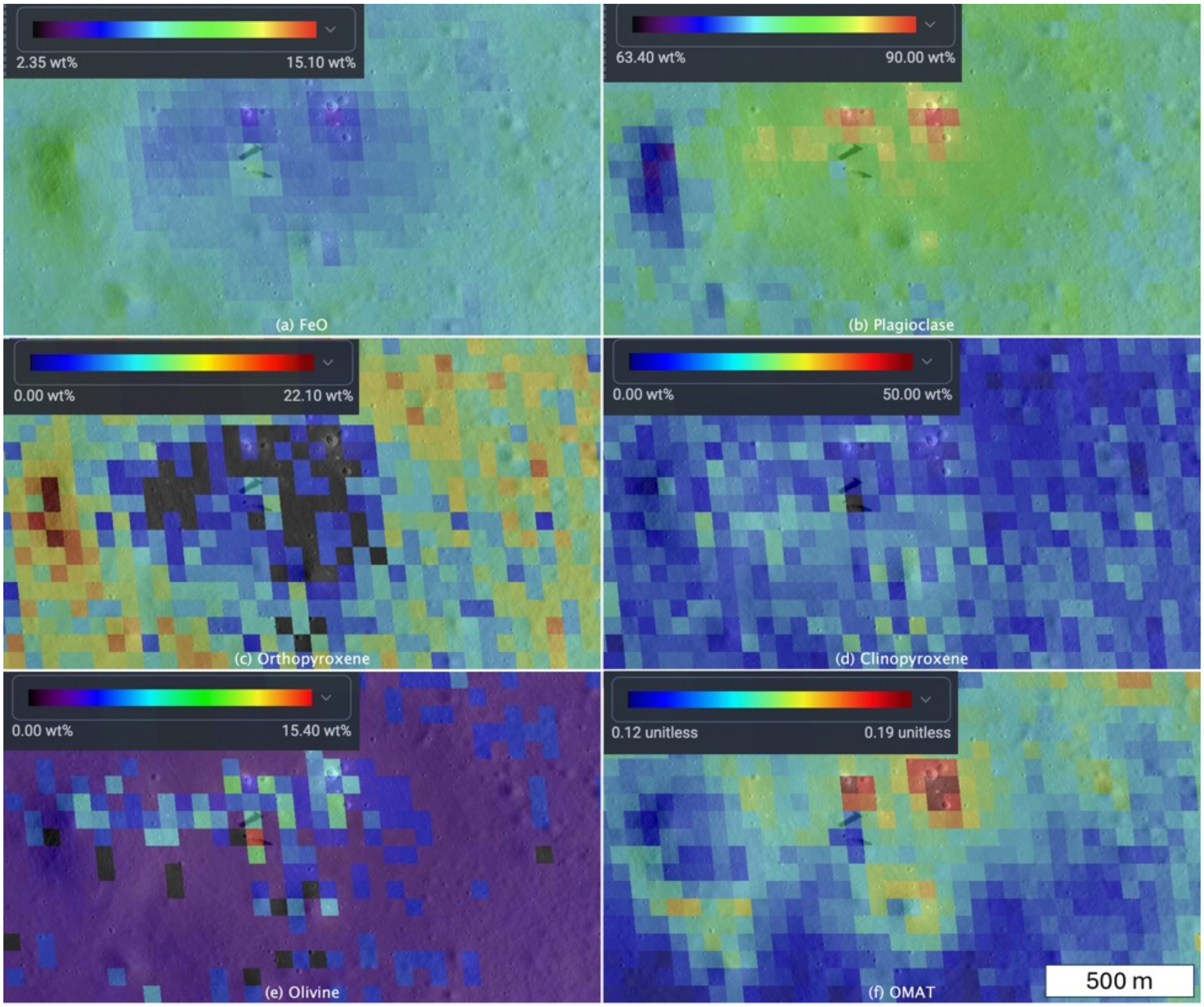

Figure 11 QuickMap Kaguya compositional layers over ~2 x 1.2 km region surrounding the features of interest. Abundance of FeO (top left), plagioclase (top right), orthopyroxene (middle left), clinopyroxene (middle right), olivine (bottom left), and derived optical maturity (bottom left) derived from topographically corrected Mineral Mapper reflectance data acquired by the JAXA SELENE/Kaguya mission (Lemelin et al. 2016). Native spatial resolution is typically 59 meters per pixel (512 pixels per degree)

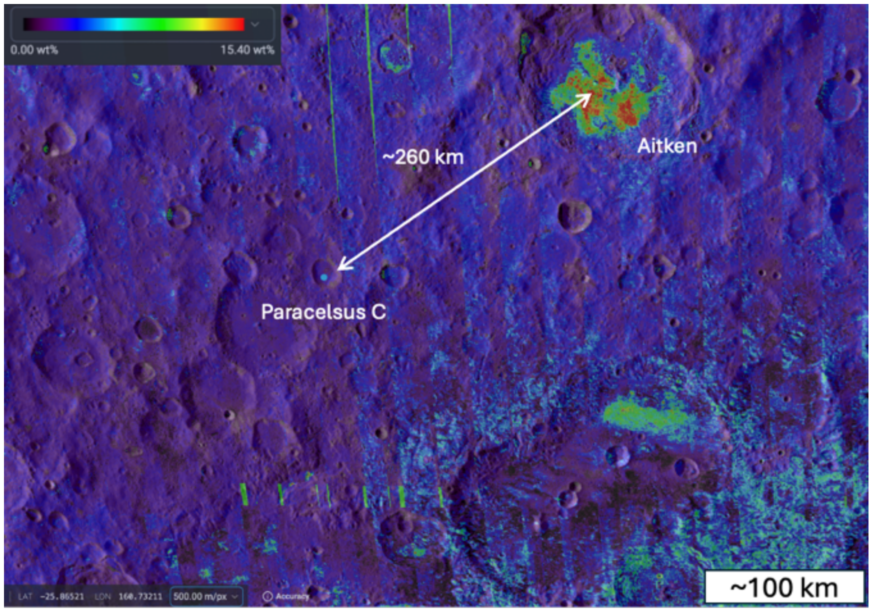

Figure 12 Olivine abundance is rare within the SP–A impact basin.

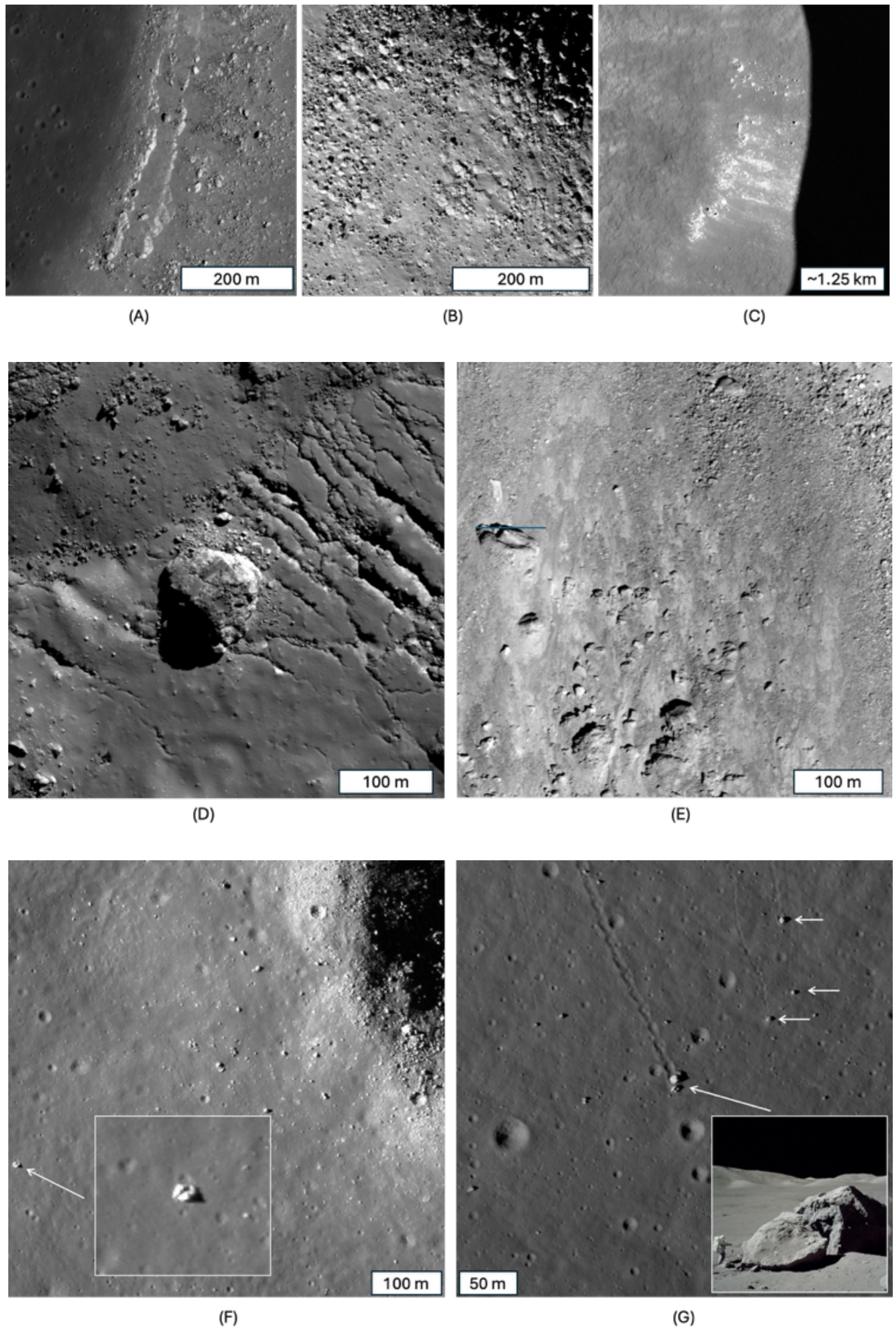

Figure 13 Lunar surface features. Exposed bedrock along Hadley Rille (A), at central uplift in Anaxagoras Crater (B), and in volcanic vent within the Schrödinger impact basin (C). Large boulder with spallation halo on the central peak of Tycho (D). Stratified ejecta block (E) on the farside. Smaller boulders in Paracelsus C (F) and at Apollo 17 Station 6 (G).

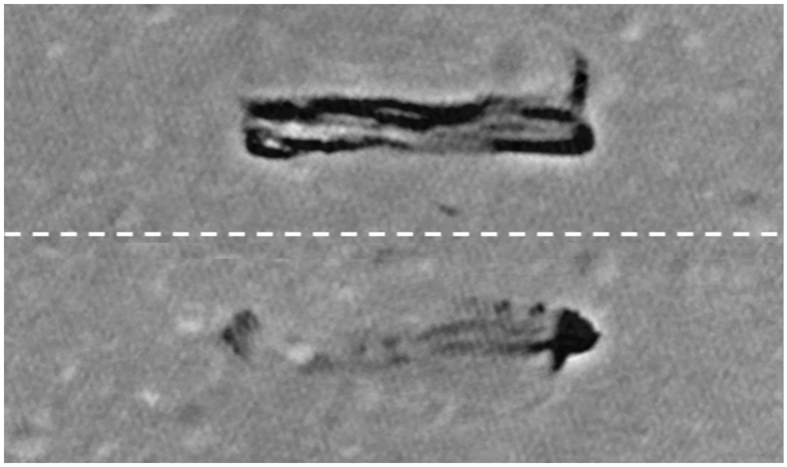

Figure 14 Contrast enhanced midday composite image with P1 placed above P2 and P3 and aligned in the same direction for comparison.

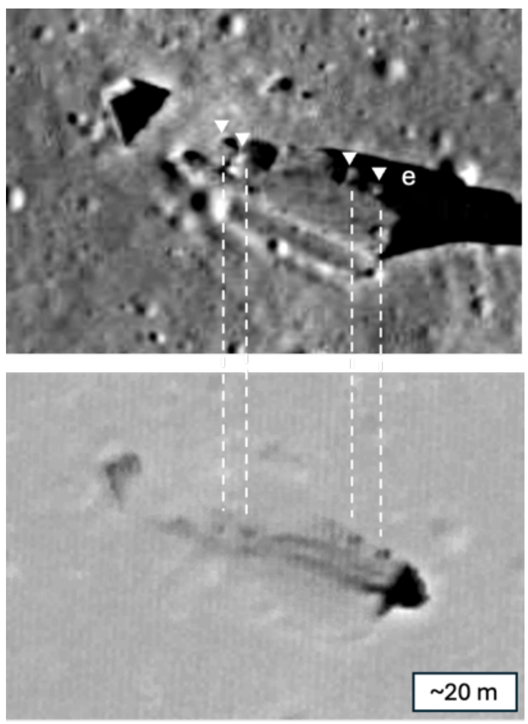

Figure 15 Fine scale details in coregistered contrast-enhanced 0.55 m/pixel afternoon image (top) and 0.96 m/pixel midday image (bottom).

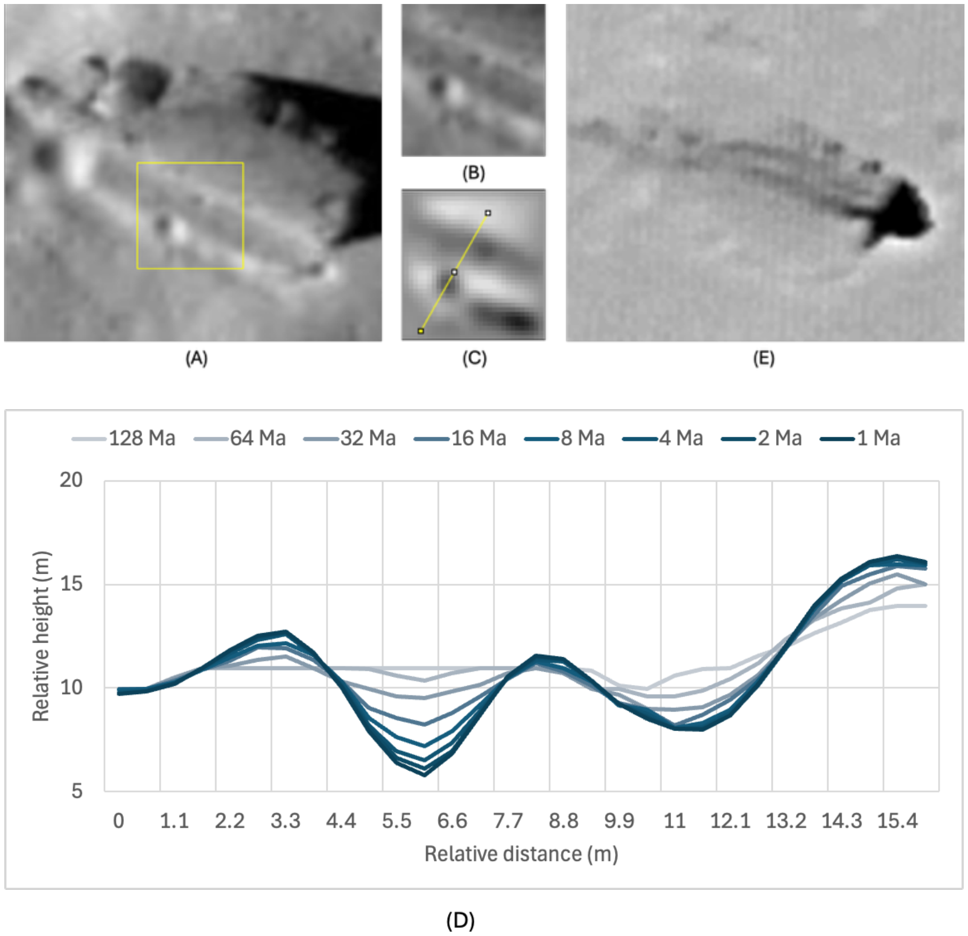

Figure 16 Topographic diffusion analysis of rille/graben and impact structures at the base of P2. Afternoon image (A), image chip (B), shape from shading height map computed from image chip and transect (C). Initial range of heights over this area ~4 m was mapped to 256 gray levels for display. Topographic diffused heights plotted along transect over timescales of 1 to 128 My assuming mare/highlands diffusivity (D). Contrast enhanced midday image (E) at same scale as (A) shown for comparison.

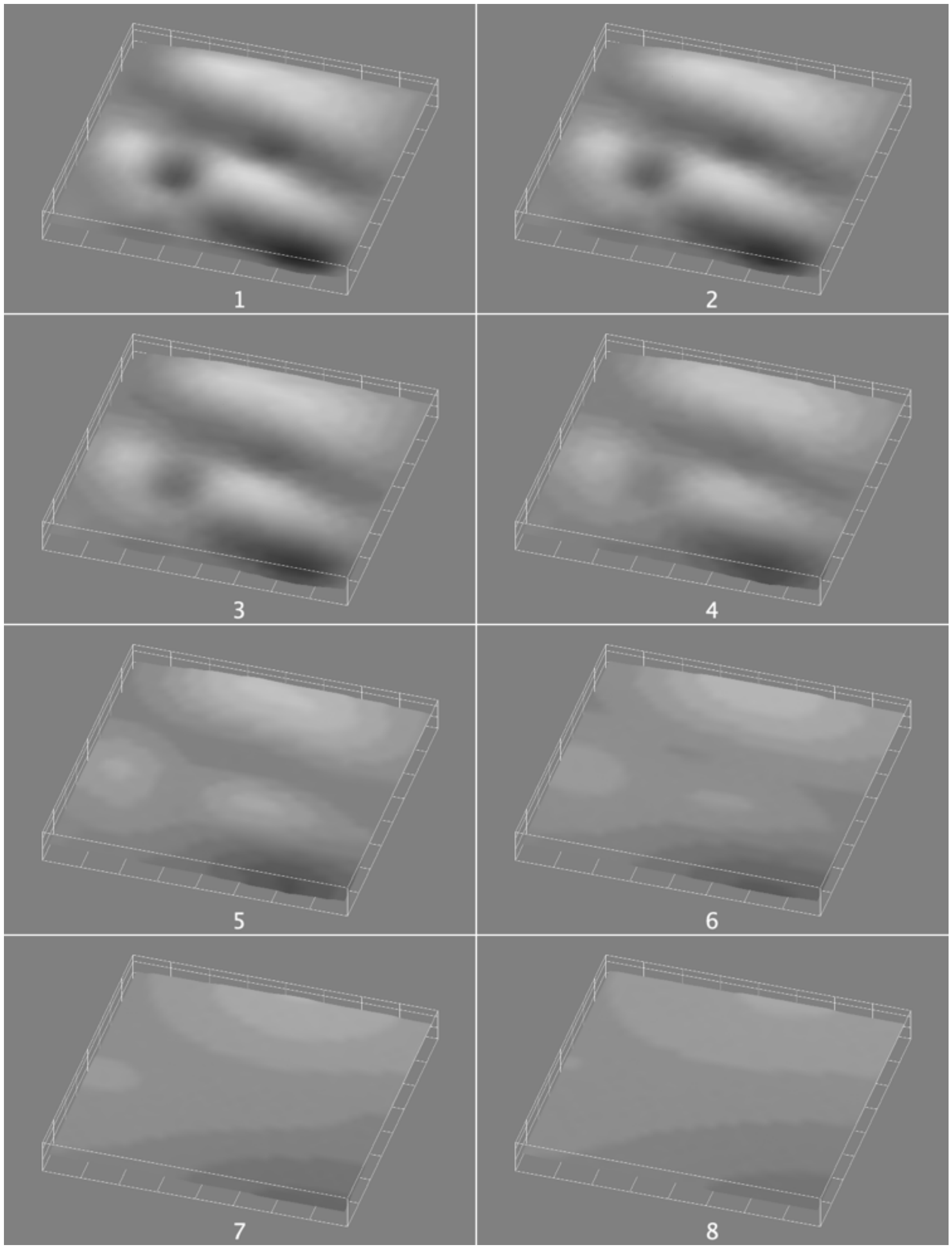

Figure 17 Topographic diffusion results for estimated topography of image chip assuming a grid spacing $\Delta x = \Delta y = 0.55$ *m/pixel, time interval* $\Delta t = 0.1$ *My, and diffusion coefficient* $\kappa = 0.109$ *m^2/My. Vertical exaggeration ~1. Surfaces labeled 1-8 show topography from N=10 iterations (1 My) at the upper left to N=1280 iterations (128 My) at the lower right. Rille/graben and nearby impact structure substantially smoothed after N=160 iterations (16 My).*

Appendix – Shape from Shading

Shape from shading (SFS), or photoclinometry, reconstructs high-resolution topography by analyzing pixel-level brightness variations in optical imagery. SFS is used here to reduce NAC-DTM processing artifacts in QuickMap terrain height data by combining QuickMap NAC-DTM with gradient information estimated from the morning, midday, and afternoon images. A variational algorithm (Horn and Brooks 1986) estimates the surface gradients p_{ij} and q_{ij} from the image E_{ij}:

$$p_{ij}^{n+1} = \bar{p}_{ij}^{n} - \tfrac{1}{2}\tilde{q}_{ij}^{n} + \frac{\varepsilon^2}{\lambda}\left[E_{ij} - R(p_{ij}^{n}, q_{ij}^{n})\right]R_p(p_{ij}^{n}, q_{ij}^{n})$$

$$q_{ij}^{n+1} = \bar{q}_{ij}^{n} - \tfrac{1}{2}\tilde{p}_{ij}^{n} + \frac{\varepsilon^2}{\lambda}\left[E_{ij} - R(p_{ij}^{n}, q_{ij}^{n})\right]R_q(p_{ij}^{n}, q_{ij}^{n})$$

where

$$\bar{p}_{ij} = \tfrac{1}{2}\left(p_{i,j+1} + p_{i,j-1}\right)$$

$$\bar{q}_{ij} = \tfrac{1}{2}\left(q_{i+1,j} + p_{i-1,j}\right)$$

$$\tilde{p}_{ij} = \tfrac{1}{4}\left(p_{i+1,j+1} + p_{i-1,j-1} - p_{i+1,j-1} - p_{i+1,j-1}\right)$$

$$\tilde{q}_{ij} = \tfrac{1}{4}\left(q_{i+1,j+1} + q_{i-1,j-1} - q_{i+1,j-1} - q_{i+1,j-1}\right)$$

$R(p, q)$ is the reflectance map, R_p and R_q are partial derivatives with respect to p and q, ε is a pixel spacing parameter, and λ is a factor that weights the relative contributions of the brightness error and smoothness. The reflectance map is the photometric model developed by Hapke (1963) and used by Horn (1990) in his study of lunar terrain. Albedo is assumed constant over the image.

A depth from gradient algorithm (Horn and Brooks 1986) computes a fused height map Z_{ij} from the above gradients by substituting QuickMap terrain heights z_{ij} at intermediate pixel locations spaced K pixels apart

$$Z_{ij}^{n+1} = \begin{cases} z_{ij}, i \ (\mathrm{mod}\, K) = j \ (\mathrm{mod}\, K) = 0 \\ \bar{Z}_{ij}^{n} - \frac{\varepsilon}{4}\left(p_{i+1,j} - p_{i-1,j} - q_{i,j+1} + q_{i,j-1}\right), \text{otherwise} \end{cases}$$

where

$$\bar{Z}_{ij} = \frac{1}{4}(Z_{i+1,j} + Z_{i-1,j} + Z_{i,j+1} + Z_{i,j-1})$$

at each iteration. This forces the resultant height map to match the QuickMap terrain heights at those locations. Parameter values were adjusted to achieve a compromise between maintaining NAC-DTM accuracy overall while reducing visual artifacts along P1 ($\lambda = 32$, and $K = 8$, $\varepsilon = 4$ for the lower resolution morning and midday images, and $\varepsilon = 2$ for the higher resolution afternoon image).

Estimated height maps after 1000 iterations are shown in Figure 18. While all three visually reduce NAC-DTM artifacts along F1 (Figure 19), the average of the morning and afternoon SFS height maps, which had the lowest RMS error (0.21 m) relative to NAC_DTM over this area, was used in the terrain visualization experiments.

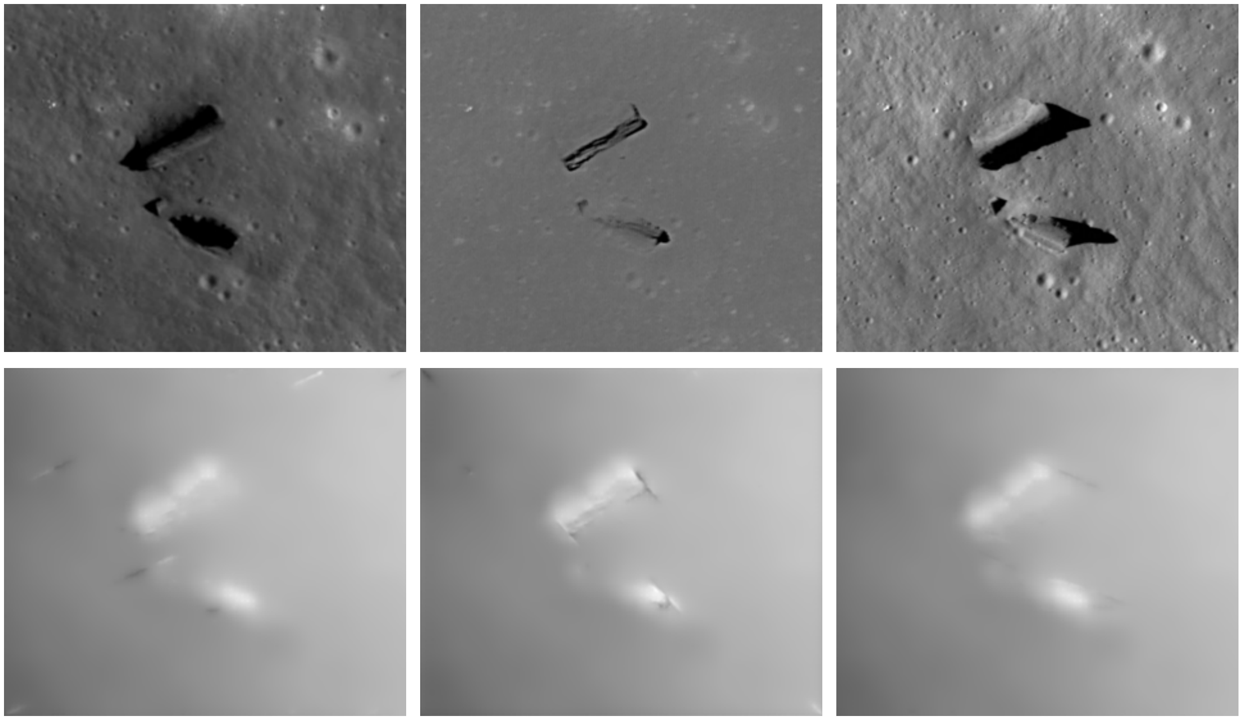

Figure 18 Morning, midday, and after LROC images (top) and SFS generated height maps (bottom).

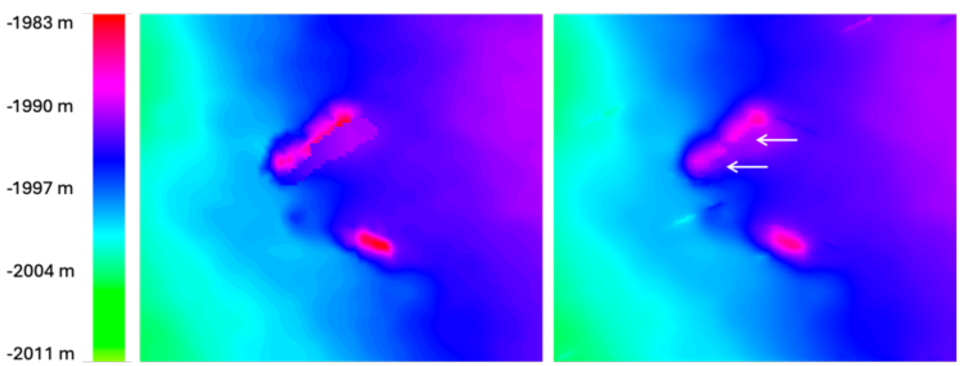

Figure 19 QuickMap height map (left) and SFS generated height map (right) with reduced edge artifacts along P1 indicated.